Supporting Information

Dual crystalline-amorphous salen-metal complexes behave like nematic droplets with AIEgens vistas

Madalin Damoc, Alexandru-Constantin Stoica, Mihaela Dascalu, Mihai Asandulesa, Sergiu Shova, Maria Cazacu*

Structural characterization

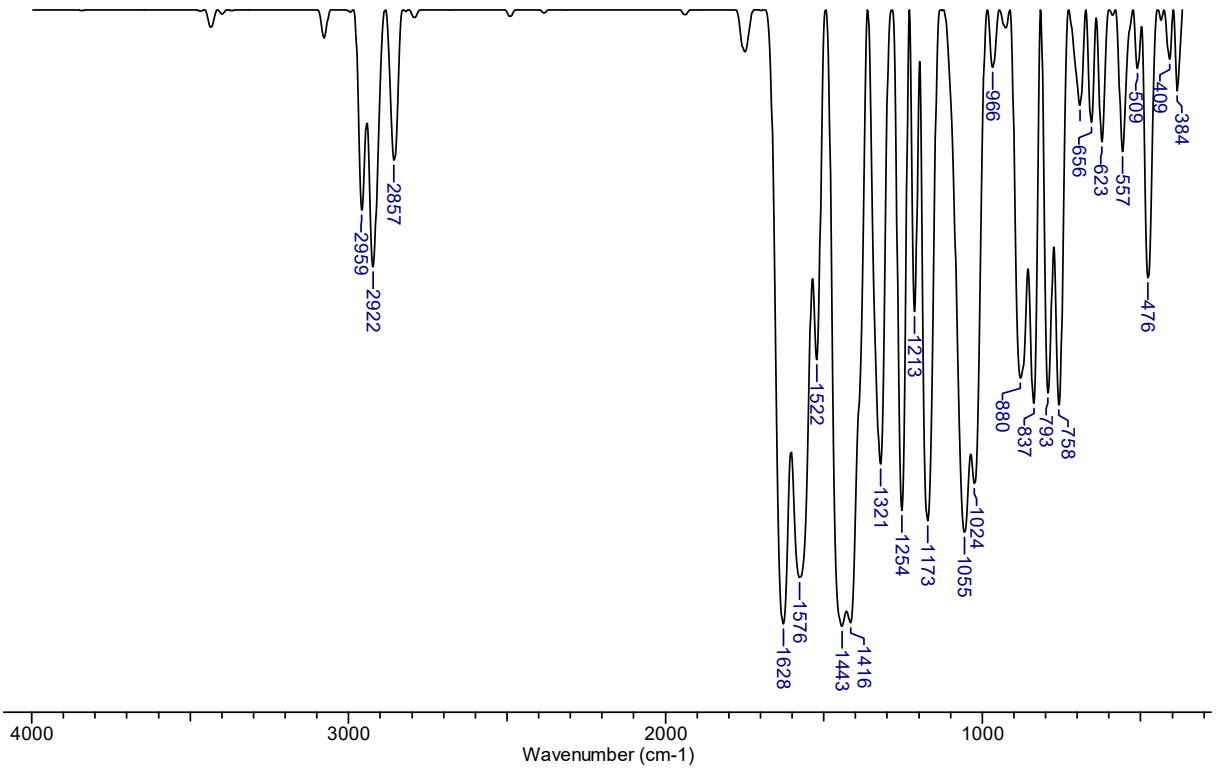

Figure S1. FTIR spectrum for CuL[1].

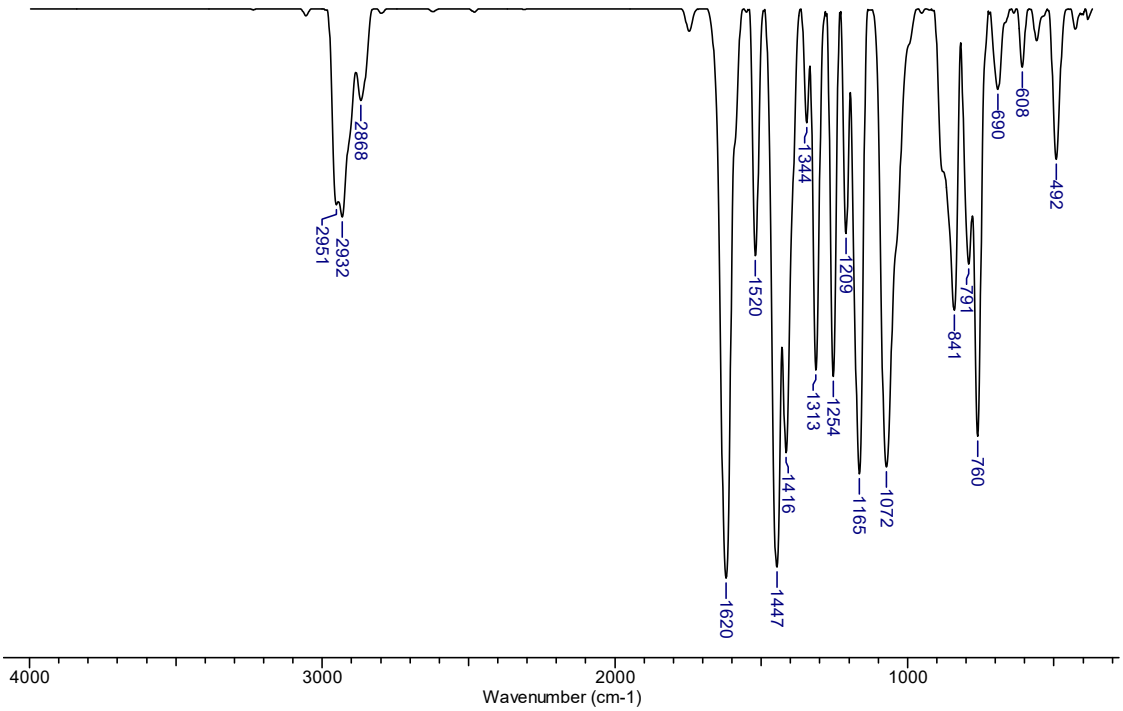

Figure S2. FTIR spectrum for ZnL[1].

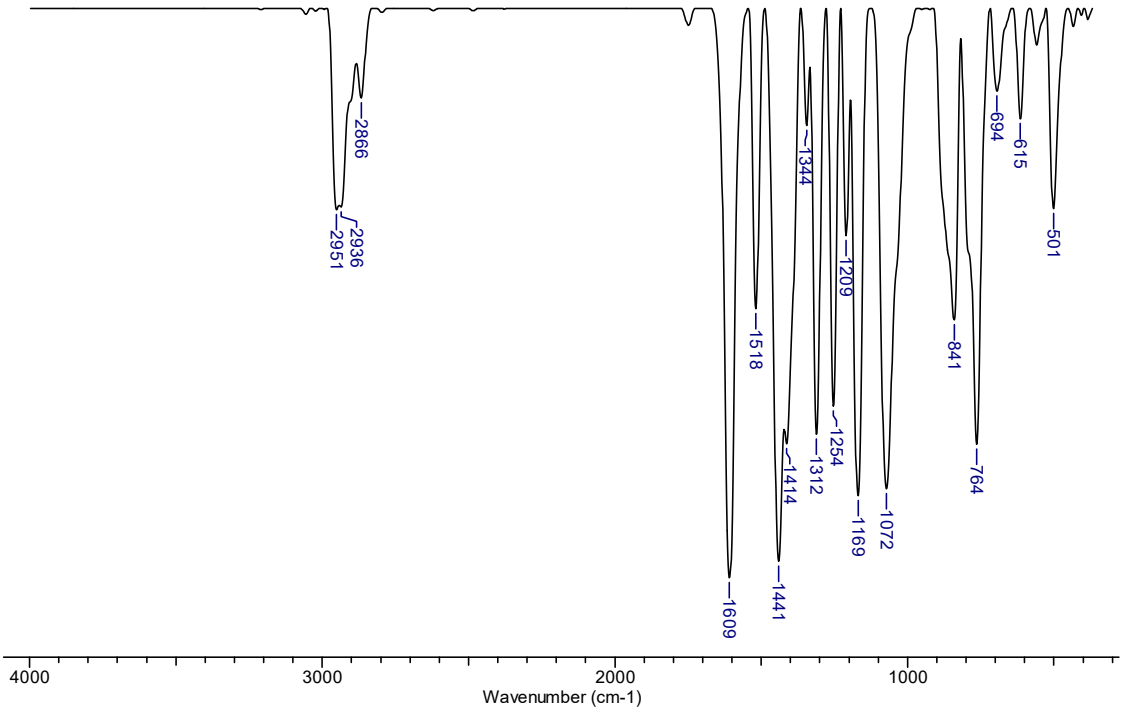

Figure S3. FTIR spectrum for CoL[1].

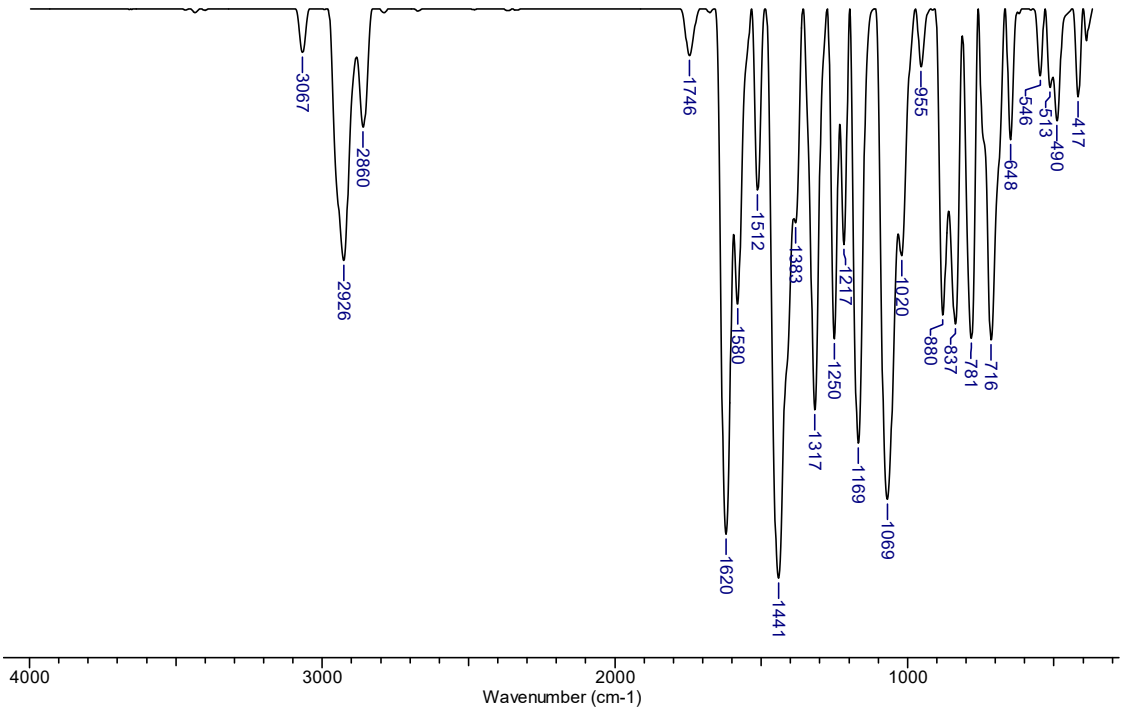

Figure S4. FTIR spectrum for NiL[1].

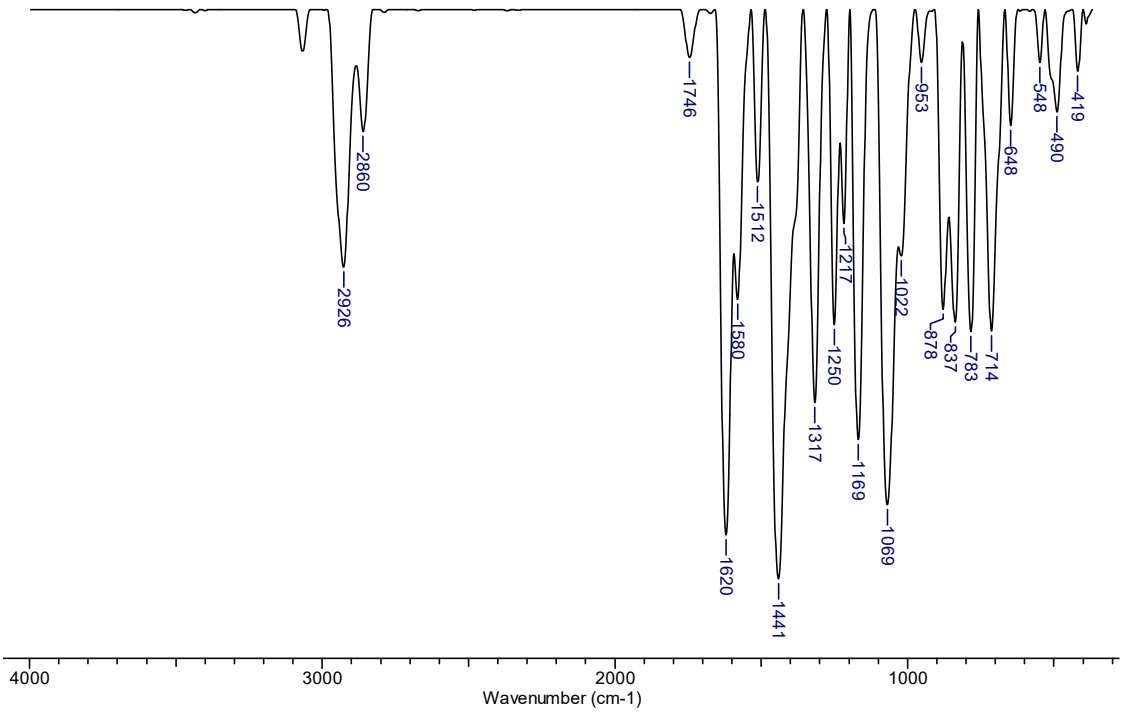

Figure S5. FTIR spectrum for NiL[2].

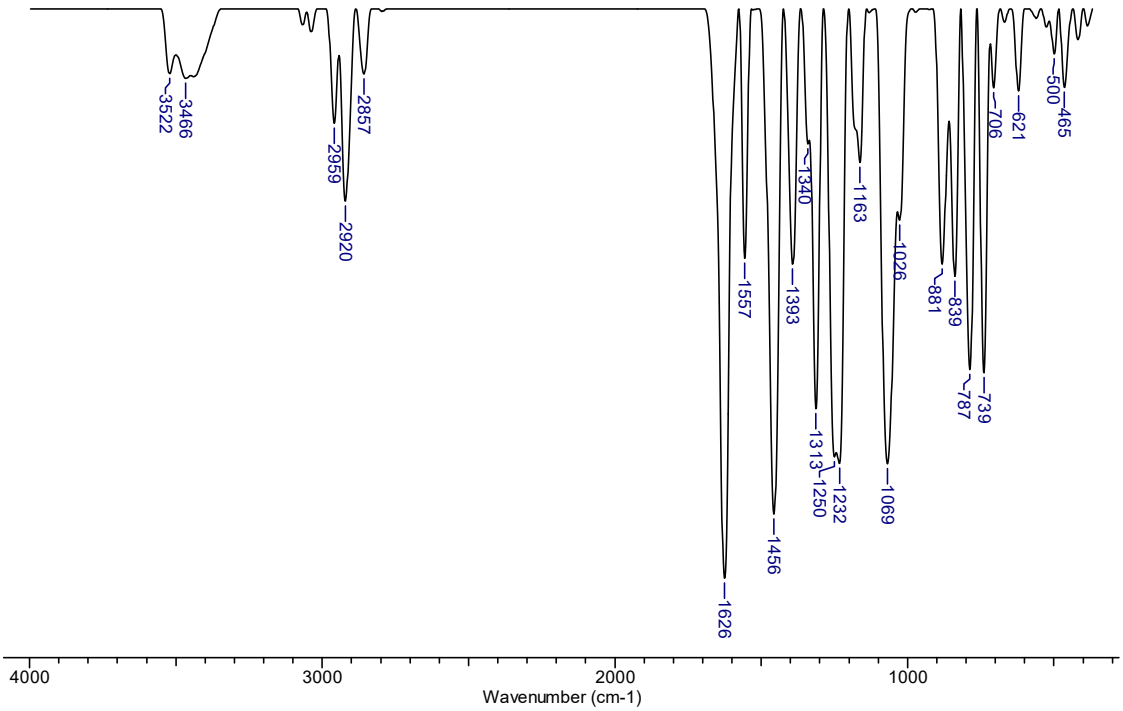

Figure S6. FTIR spectrum for CuL^3.

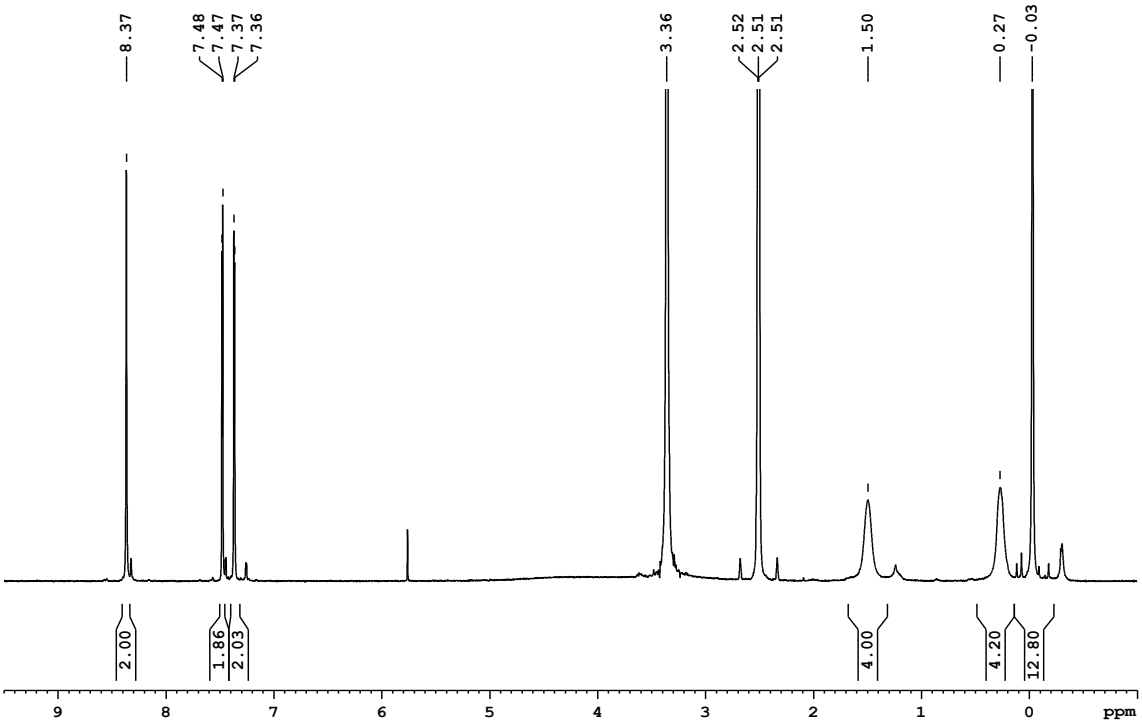

Figure S7. ^{1}HNMR spectrum for ZnL^1.

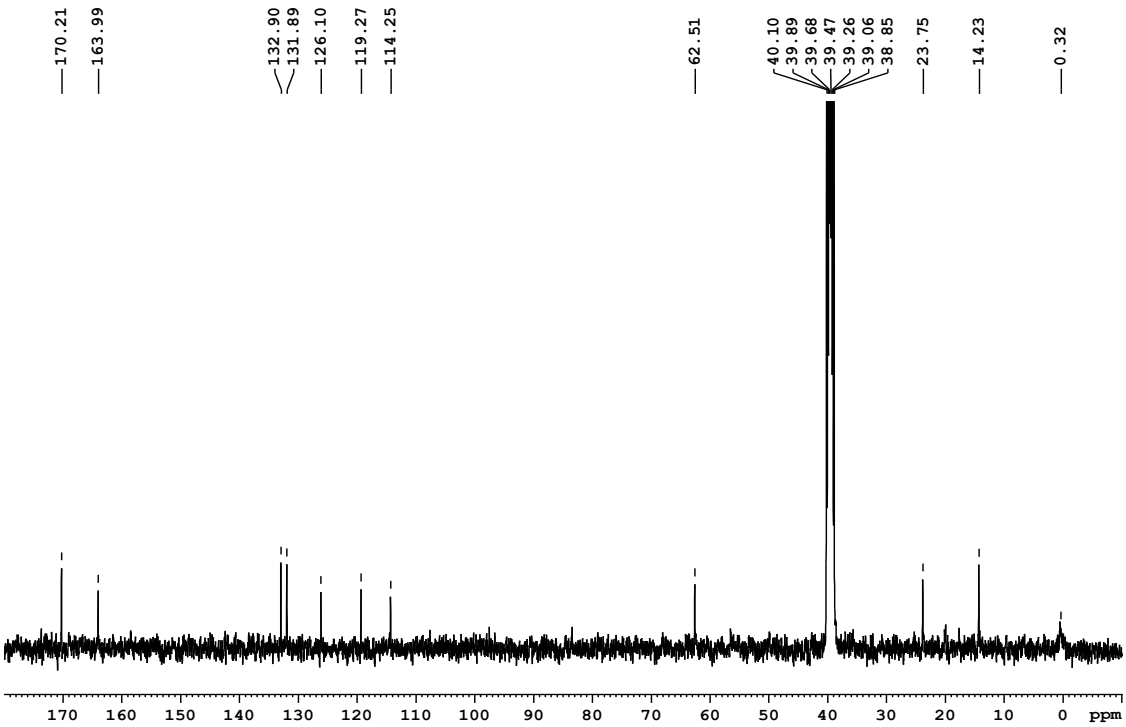

Figure S8. ^{13}CNMR spectrum for ZnL^1.

Crystallographic analysis

Tabel S1. Crystal data and details of data collection for complexes**.**

Compound	**NiL^1**	**CuL^1**	**CoL^1**
empirical formula	$C_{48}H_{60}Cl_8N_4Ni_2O_6Si_4$	$C_{49}H_{62}Cl_{10}Cu_2N_4O_6Si_4$	$C_{73}H_{92}Cl_{14}Co_3N_6O_9Si_6$
Fw	1302.38	1396.96	2039.15
space group	$P2_1/c$	$P2_1/c$	P-1
a [Å]	15.2553(12)	20.1918(12)	15.6932(7)
b [Å]	23.7162(17)	12.5700(9)	17.4257(10)
c [Å]	17.6798(13)	26.0592(14)	19.5315(9)
α [°]	90	90	99.440(4)
β[°]	108.105(9)	103.639(6)	104.592(4)
γ [°]	90	90	109.205(5)
V [Å^3]	6079.8(8)	6427.6(7)	4699.7(4)
Z	4	4	2
ρ_{calcd} [g cm^{-3}]	1.423	1.444	1.441
Crystal size [mm]	0.5 × 0.4 × 0.2	0.6 × 0.15 × 0.05	0.5 × 0.05 × 0.03
T [K]	293(2)	180.05(10)	180.1(2)
μ [mm^{-1}]	1.097	1.198	1.051
2Θ range	2.97 to 50.05	3.216 to 50.054	3.622 to 50.052
Reflections collected	31505	31162	37110
Independent	10737 [R_{int} = 0.0686]	11343 [R_{int} = 0.0558]	16537 [R_{int} = 0.0720]
Data/restraints/para	10737/9/653	11343/2/686	16537/0/1012

R_1[a]	0.0731	0.0598	0.0515
wR_2[b]	0.1486	0.1239	0.0845
GOF[c]	1.037	1.039	0.838
Largest diff.	0.46/-0.39	0.77/-0.89	0.57/-0.55

Compound	**ZnL[1]**	**NiL[2]**	**CuL[3]**
empirical formula	$C_{73}H_{92}Cl_{14}Zn_3N_6O_9Si_6$	$C_{48}H_{60}Br_8N_4Ni_2O_6Si_4$	$C_{48}H_{68}Cu_2N_4O_{10}Si_4$
Fw	2058.47	1658.06	1100.50
space group	P-1	$P2_1/c$	$P2_1/c$
a [Å]	15.6914(9)	15.4499(13)	14.9833(18)
b [Å]	17.4652(7)	23.9712(14)	14.3565(11)
c [Å]	19.6006(8)	17.9196(12)	26.913(2)
α [°]	99.587(3)	90	90
β [°]	104.598(4)	109.483(8)	96.812(10)
Γ [°]	109.175(4)	90	90
V [Å^3]	4723.6(4)	6256.6(8)	5748.3(9)
Z	2	4	4
ρ_{calcd} [g cm^{-3}]	1.447	1.760	1.272
Crystal size [mm]	0.4 × 0.15 × 0.08	0.2 × 0.15 × 0.05	0.15 × 0.15 × 0.04
T [K]	180.05(10)	180.00(10)	293(2)
μ [mm^{-1}]	1.280	5.833	0.877
2Θ range	3.028 to 50.054	3.398 to 50.054	3.22 to 50.054
Reflections collected	35173	30414	21695
Independent	16648 [R_{int} = 0.0547]	11048 [R_{int} = 0.0666]	10133 [R_{int} = 0.1250]
Data/restraints/para	16648/2/1019	11048/3/652	10133/24/625
R_1[a]	0.0823	0.0514	0.0676
wR_2[b]	0.1753	0.0843	0.1265
GOF[c]	1.099	0.888	0.845
Largest diff.	0.73/-0.75	0.87/-1.17	0.33/-0.36

[a]$R_1 = \Sigma||F_o| - |F_c||/\Sigma|F_o|$. [b]$wR_2 = \{\Sigma[w(F_o^2 - F_c^2)^2]/\Sigma[w(F_o^2)^2]\}^{1/2}$. [c]$GOF = \{\Sigma[w(F_o^2 - F_c^2)^2]/(n - p)\}^{1/2}$, where n is the number of reflections and p is the total number of parameters refined.

Tabel S2. Selected bond lengths [Å] and angles [°] for complexes.

	NiL[1]		**CuL[1]**		**NiL[2]**		**CuL[3]**	
	A	**B**	**A**	**B**	**A**	**B**	**A**	**B**
M1-O1	1.834(4)	1.848(4)	1.893(3)	1.896(3)	1.827(5)	1.852(4)	1.897(4)	1.897(5)
M1-O2	1.845(4)	1.826(4)	1.896(3)	1.905(3)	1.856(4)	1.832(4)	1.918(5)	1.898(5)
M1-N1	1.909(4)	1.913(5)	1.965(4)	1.971(4)	1.901(5)	1.889(6)	1.956(6)	1.979(6)
M1-N2	1.895(5)	1.890(4)	1.955(4)	1.971(4)	1.897(5)	1.905(6)	1.973(6)	1.982(6)
Si1-O3	1.607(4)	1.598(5)	1.616(3)	1.623(4)	1.616(5)	1.625(5)	1.590(5)	1.601(5)
Si2-O3	1.612(4)	1.602(5)	1.627(4)	1.626(4)	1.599(5)	1.614(5)	1.618(6)	1.606(6)
O1-M1-O2	168.96(16)	92.8(2)	163.43(15)	162.33(13)	165.9(2)	94.1(2)	156.1(2)	157.2(2)
O1-M1-N1	92.27(19)	88.94(19)	92.25(15)	93.12(14)	93.1(2)	87.2(2)	93.2(2)	93.0(3)
O1-M1-N2	88.70(19)	167.25(18)	89.30(14)	88.82(14)	87.3(2)	169.03(18)	90.5(2)	91.1(3)

O2-M1-N1	86.81(19)	87.5(2)	90.01(14)	92.73(15)	89.5(2)	87.9(2)	94.7(3)	93.4(3)
O2-M1-N2	94.09(19)	93.28(18)	92.47(13)	91.38(14)	93.1(2)	92.8(2)	92.4(3)	92.7(3)
N2-M1-N1	170.17(17)	168.41(19)	165.97(17)	159.92(15)	167.7(2)	170.3(2)	153.2(3)	154.1(3)
Si1-O3-Si2	161.7(3)	163.7(4)	160.9(3)	154.5(2)	166.0(5)	159.9(3)	157.1(4)	163.9(4)
τ_4'[a]	0.144	0.169	0.209	0.260	0.182	0.143	0.351	0.336

	CoL[1]			**ZnL[1]**		
	A	**B**	**C**	**A**	**B**	**C**
M1-O1	1.904(3)	1.899(3)	1.906(3)	1.908(5)	1.924(4)	1.921(5)
M1-O2	1.901(3)	1.902(3)	1.911(3)	1.903(4)	1.917(5)	1.940(5)
M1-N1	1.999(3)	1.988(3)	1.981(3)	1.999(5)	1.994(5)	1.989(5)
M1-N2	1.984(3)	1.979(3)	1.998(3)	2.010(5)	1.985(5)	2.018(5)
Si1-O3	1.612(3)	1.622(3)	1.627(3)	1.617(6)	1.626(5)	1.638(5)
Si2-O3	1.613(3)	1.614(3)	1.625(3)	1.622(6)	1.616(5)	1.614(5)
O1-M1-O2	125.37(12)	124.51(13)	123.62(12)	122.9(2)	120.8(2)	120.3(2)
O1-M1-N1	95.25(14)	96.34(13)	96.41(13)	95.2(2)	96.4(2)	97.1(2)
O1-M1-N2	103.54(13)	104.16(13)	108.62(13)	101.9(2)	104.4(2)	108.8(2)
O2-M1-N1	106.42(13)	107.02(12)	107.02(13)	107.4(2)	106.7(2)	106.6(2)
O2-M1-N2	95.87(13)	97.47(13)	95.69(14)	95.5(2)	97.8(2)	96.2(2)
N2-M1-N1	134.40(13)	130.57(14)	128.35(13)	137.4(2)	133.4(2)	130.0(2)
Si1-O3-Si2	163.3(2)	159.0(2)	155.6(2)	160.9(4)	159.4(3)	155.6(3)
τ_4'	0.683	0.725	0.752	0.662	0.711	0.748

[a] $\tau_4' = \frac{\beta - \alpha}{360 - \theta} + \frac{180 - \beta}{180 - \theta}$, where α and β are the two largest valence angles at the M atom, and θ = 109.5°.

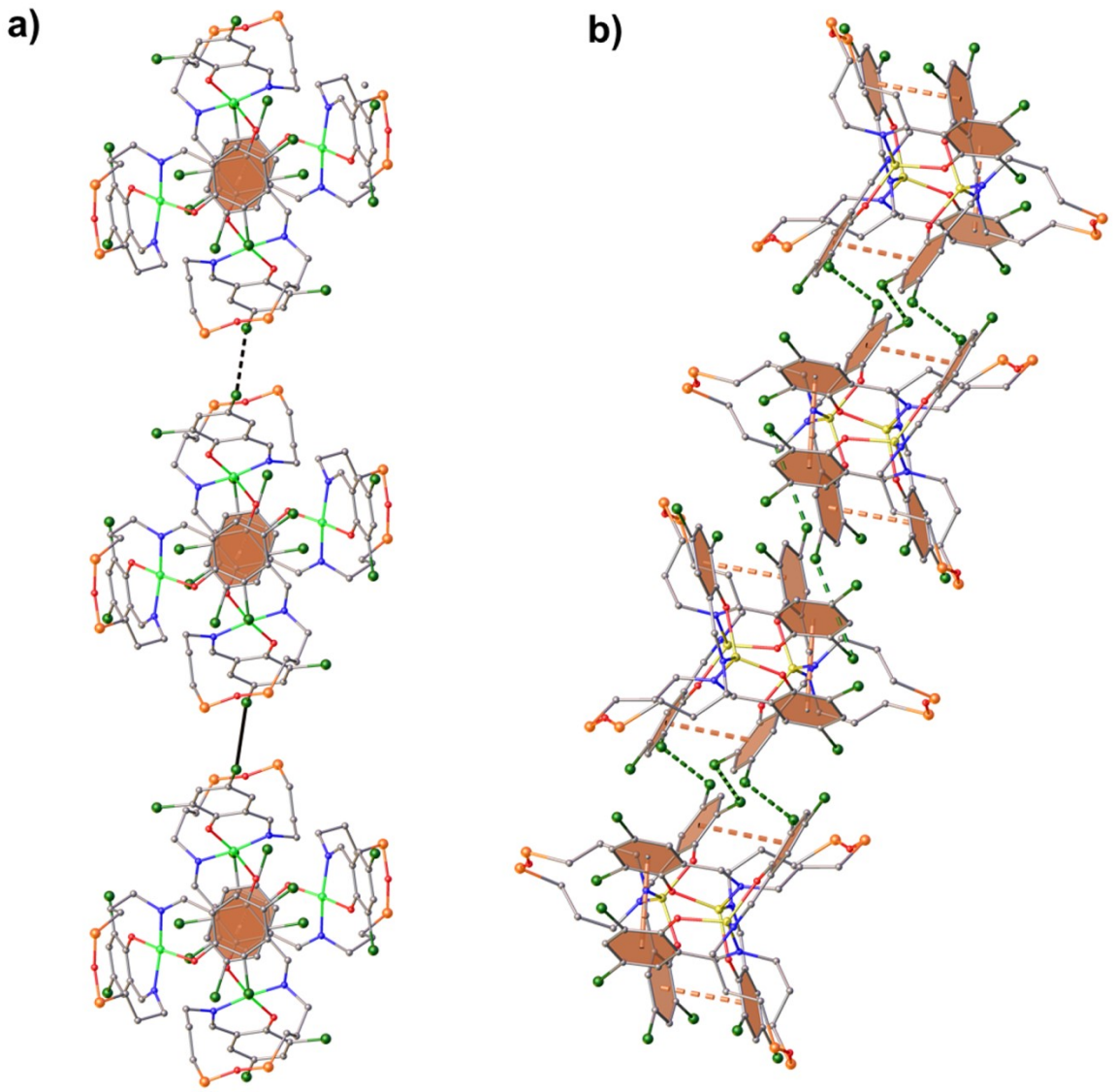

Figure S9. 2D supramolecular layers in NiL^1 (a) and ZnL^1 (b), viewed along plane.

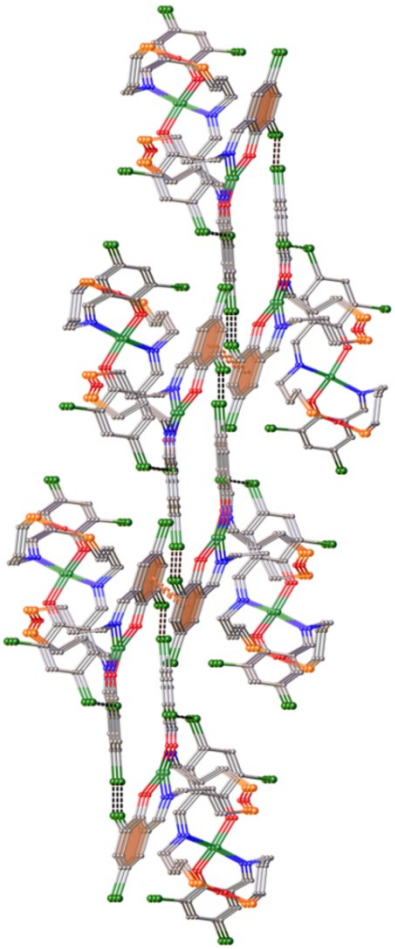

Figure S10. 2D supramolecular layers in CuL^1 viewed along plane.

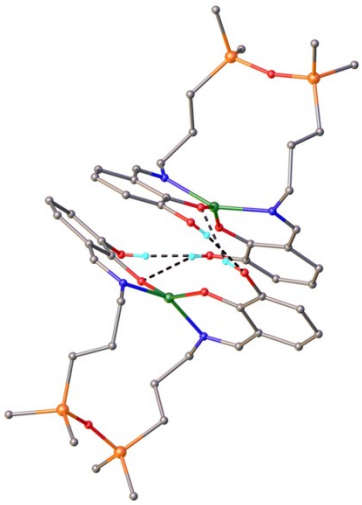

Figure S11. Intermolecular hydrogen bonding in the crystal structure of CuL^3 (right side). H-bond parameters: O2A-H···O4B [O2A-H 0.87Å, H···O4B 2.03Å, O2A···O4B 2.765(7)Å, ∠O2AHO4B 142.5]; O5A-H···O2B [O5A-H 0.84Å, H···O2B 2.21Å, O5A···O2B 3.048(9)Å, ∠O5AHO2B 176.2]; O2B-H···O4A [O2B-H 0.82Å, H···O4A 2.18Å, O2B···O4A 2.957(7)Å, ∠O2BHO4A 158.1]; O5B-H···O2A [O5B-H 0.82Å, H···O2A 2.20Å, O5B···O2A 3.017(8)Å, ∠O5BHO2A 174.9].

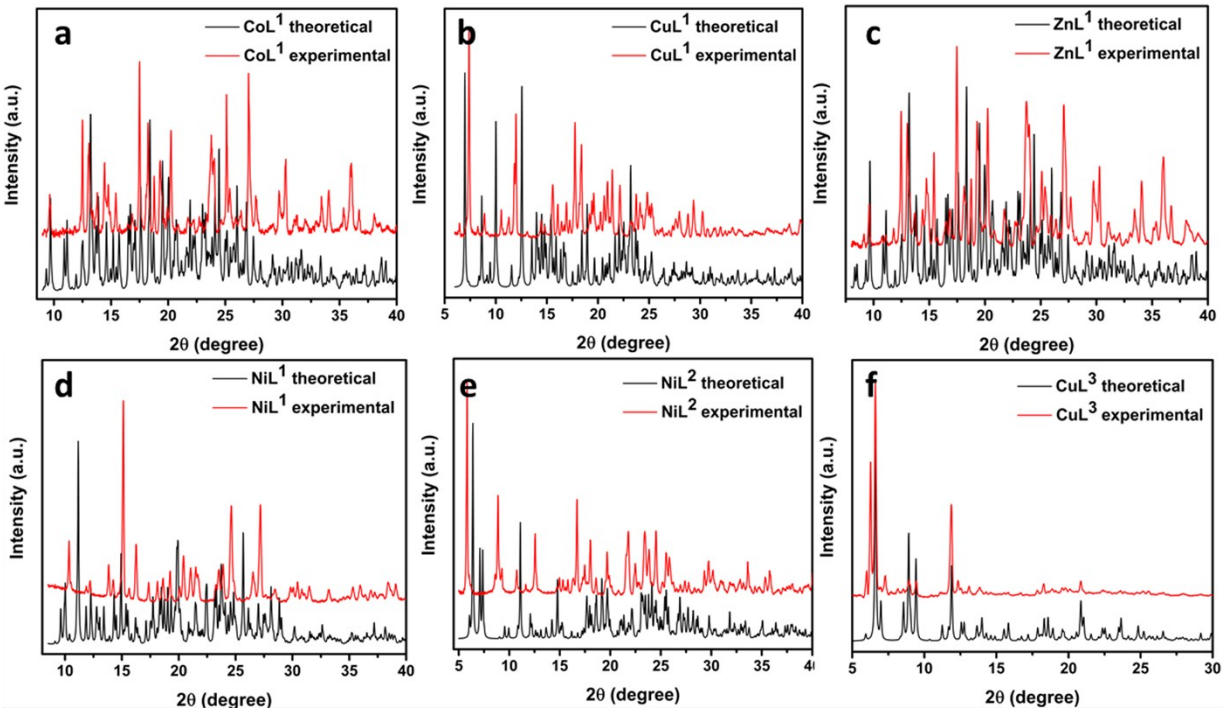

Figure S12. PXRD data for metal complexes: CoL^1 (a), CuL^1 (b), ZnL^1 (c), NiL^1 (d), NiL^2 (e) and CuL^3 (f).

Thermal analysis

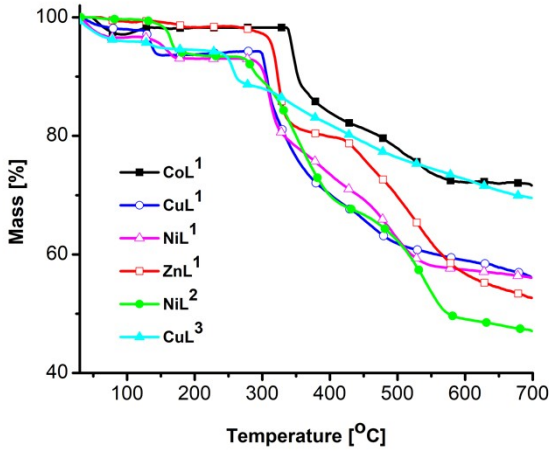

Figure S13. Thermogravimetric analysis for all complexes presenting three main degradation stages starting with 300 °C. The small mass changes until 200 °C, are assigned due the solvent losses.

Table S3. Thermal degradation stages extracted from thermogravimetric analysis.

Compound	Stage of thermal degradation	T_{onset}	T_{peak}	T_{endset}	Mass losses %	The residue amount at 700 °C %
ZnL[1]	I	29.52	51.18	73.91	15.41	49.09
	II	143.65	178.51	188.66	2.28	
	III	316.7	331.03	339.02	10.68	
	IV	432.48	492.17	573.95	22.22	
NiL[1]	I	31.53	43	79.07	7.43	54.08
	II	142.84	153.68	165.39	2.15	
	III	286.88	308.68	322.96	23.45	
	IV	453.02	486.64	538.5	11.94	
CuL[1]	I	33.08	45.11	80.14	1.71	55.85
	II	125.77	134.37	143.01	3.56	
	III	299.97	307.42	312.65	8.74	
	IV	314	338.96	374.81	17.11	
	V	441.62	446.3	487.95	12.58	
CoL[1]	I	31.42	41.98	88.74	5	64.37
	II	127.03	148.1	180.73	1.76	
	III	341.86	350.31	359.56	17.91	
	IV	455.09	514.96	583.16	10.35	
NiL[2]	I	32.1	38.1	64.9	1.56	52.15
	II	151.7	164.7	170.8	5.93	
	III	272.7	284.4	292.4	4.23	
	IV	312.0	345.2	401.4	21.46	
		456.5	542.8	568.8	19.79	
CuL[3]	I	29.29	50.71	92.5	1.1	73.96
	II	129.07	154.1	168.99	1.01	
	III	237.59	251.92	263.99	3.98	
	IV	321.36	344.39	369.68	7.28	
	V	421.43	464.39	485.78	6.09	
	VI	573.09	596.76	636.41	4.84	

Liquid crystalline behavior

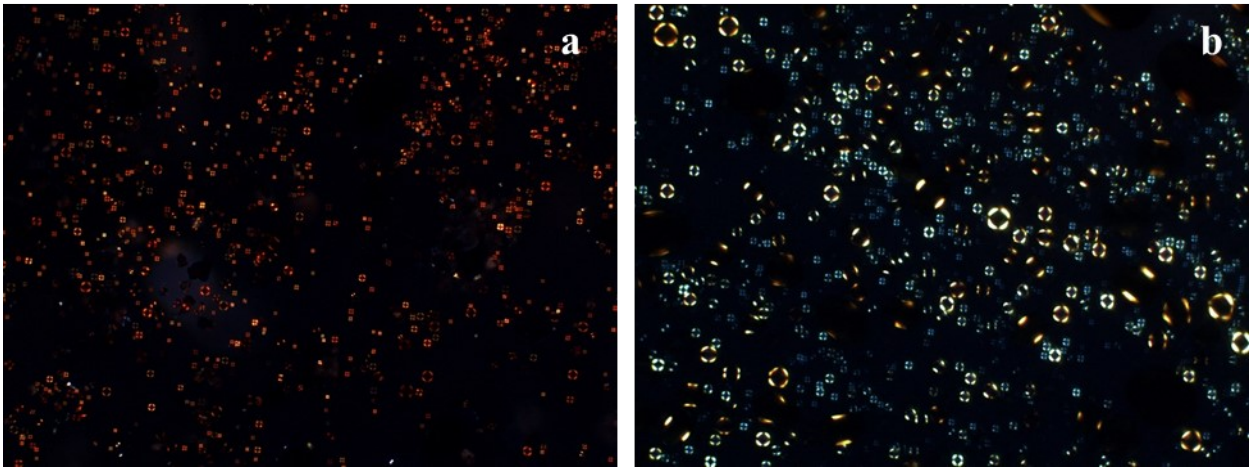

Figure S14. Nematic liquid crystals for CuL^3 (a) and NiL^1 (b).

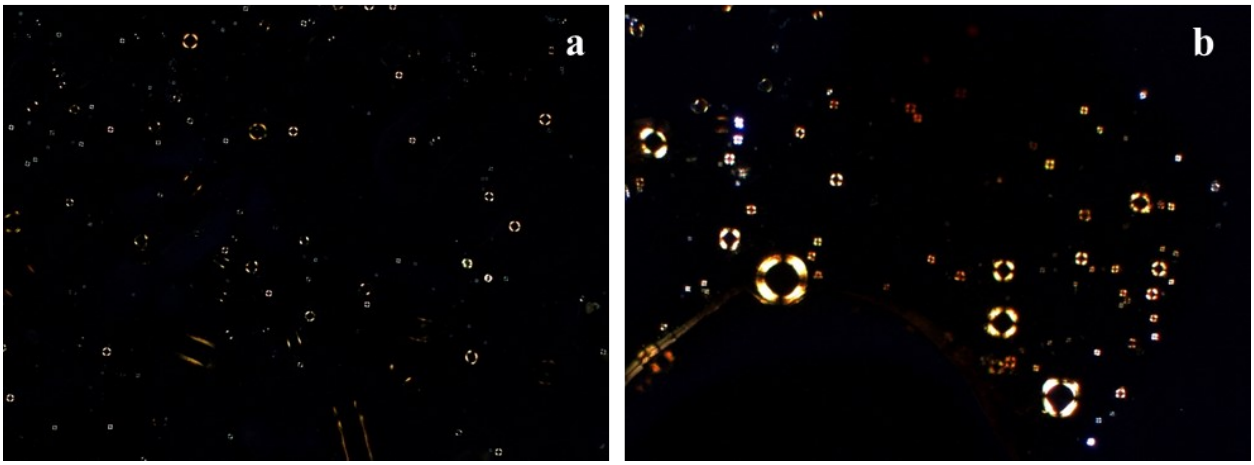

Figure S15. Nematic liquid crystals for NiL^2 (a) and CuL^1 (b).

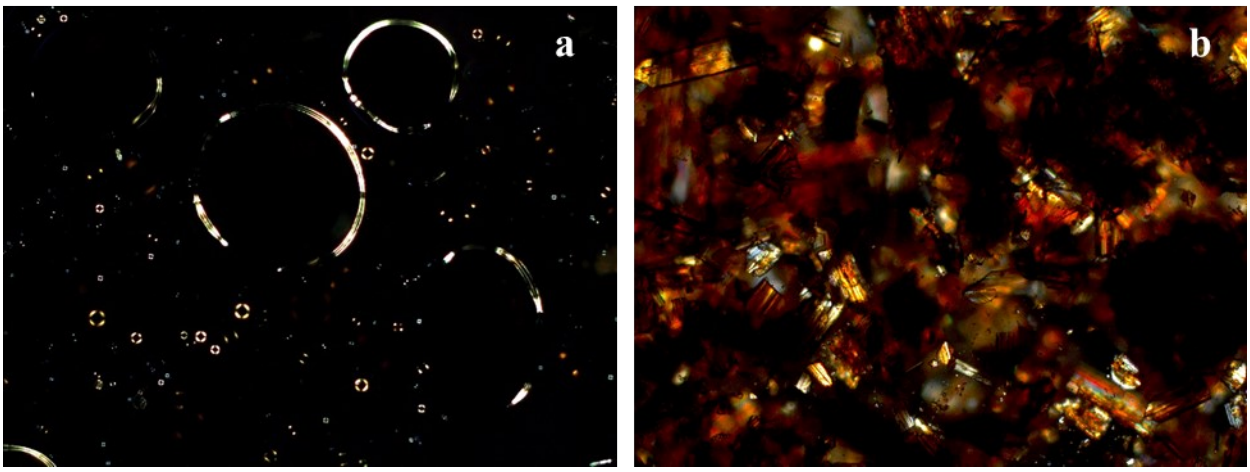

Figure S16. Nematic defects in solid state of NiL^2 (the biggest ones) (a) and NiL^2 purely crystals (b).

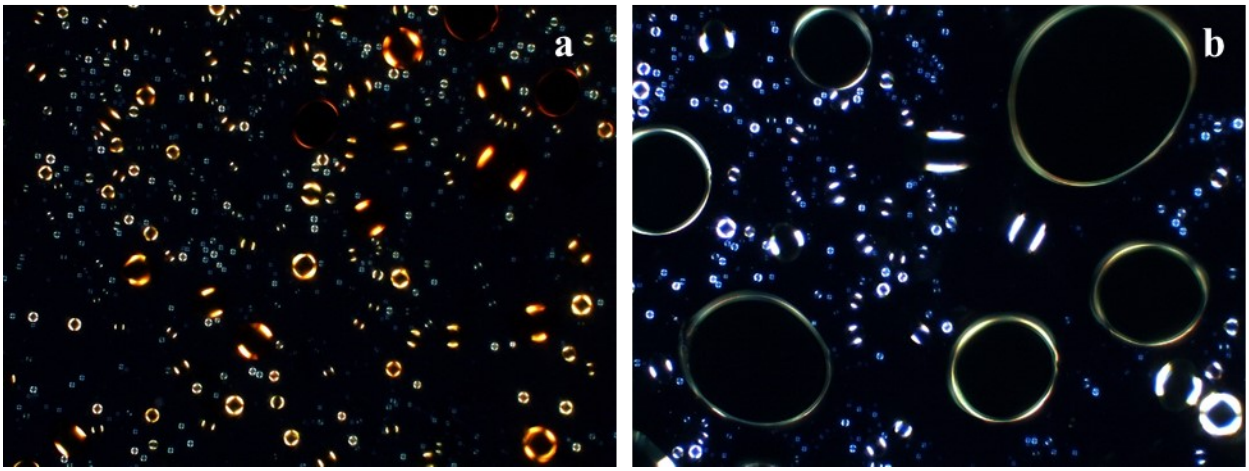

Figure S17. Nematic droplets of CoL^1 (a) and ZnL^1 (b).

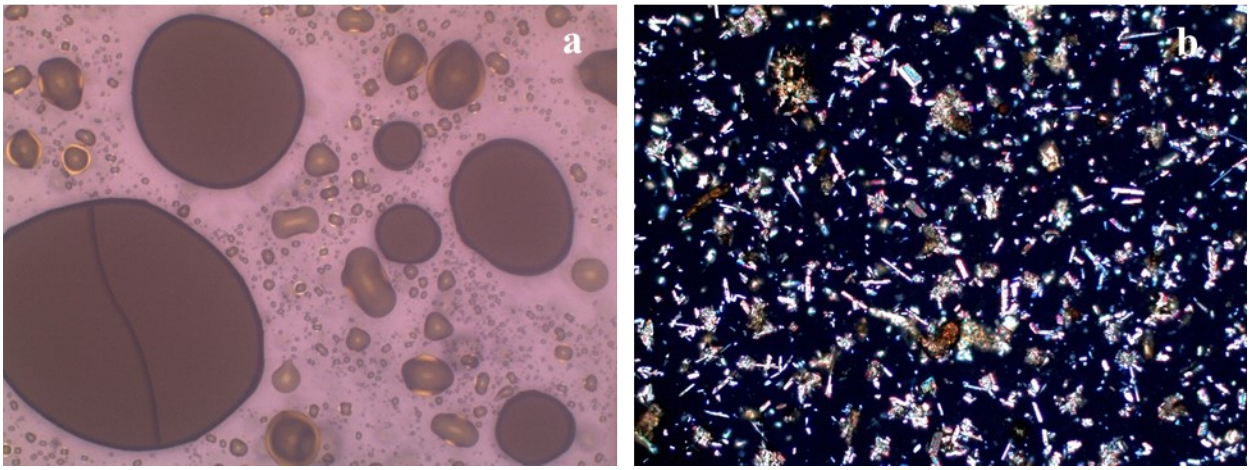

Figure S18. NiL^1 nematic glass turning in solid state at room temperature (a) and solid state purely crystals (b).

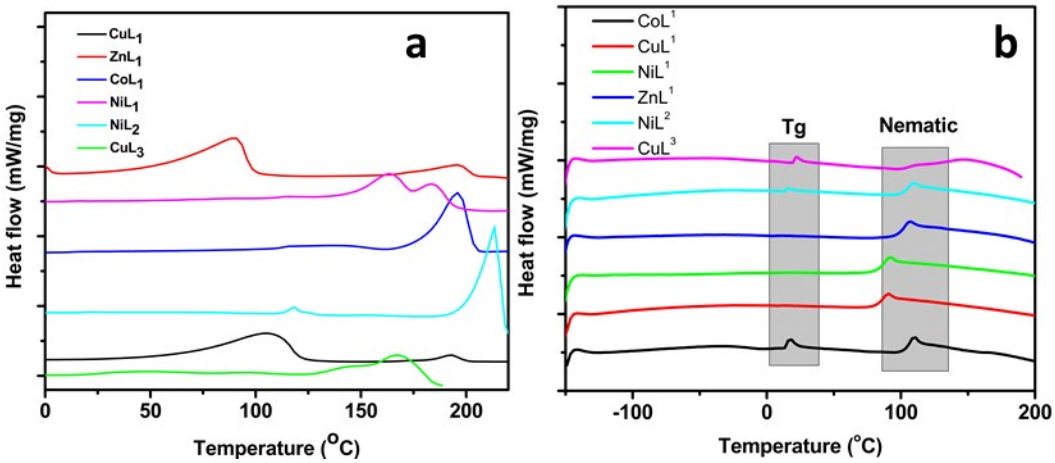

Figure S19. First heating on DSC showing three endothermic transitions: glass transition, nematic mesophase and isotropization (a); Third heating on DSC showing two endothermic transitions: glass transition and mesophase (b).

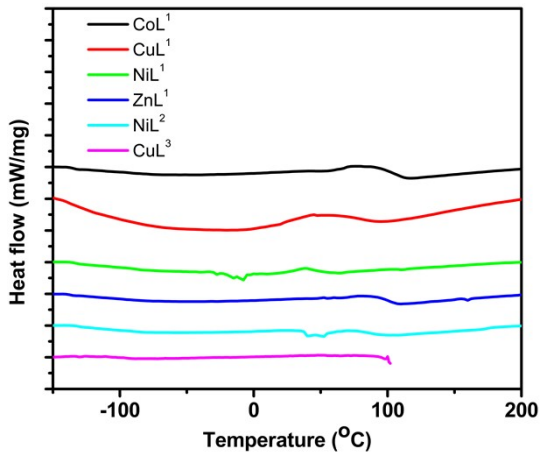

Figure S20. Cooling on DSC showing two exothermic phase transitions due to the nematic mesophase and crystallization.

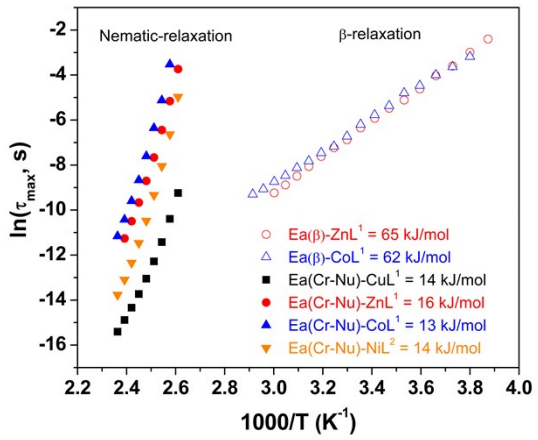

Figure S21. Arrhenius plot of β- and nematic-relaxations of complexes.

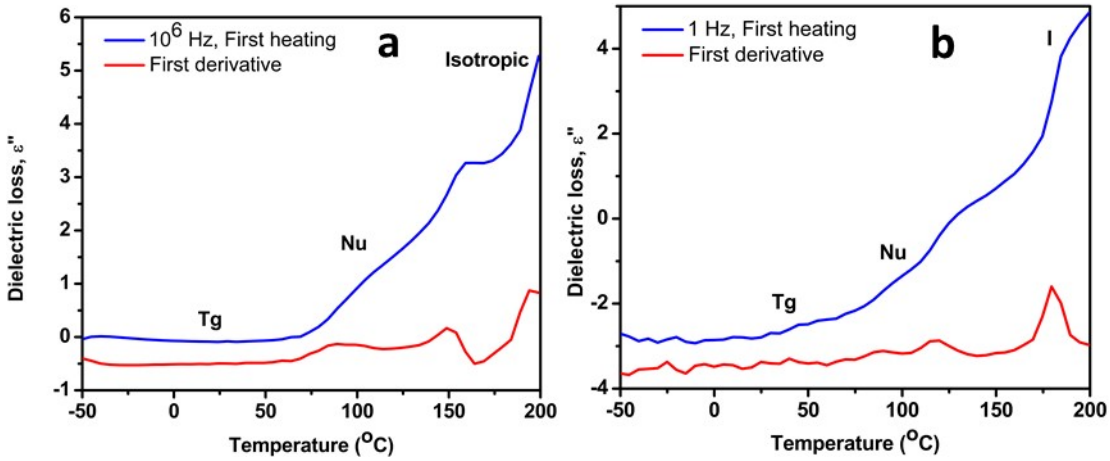

Figure S22. Phase transitions highlighted by dielectric spectroscopy for CuL^1 (a) and CoL^1 (b): Tg (glass transition), Nu (nematic uniaxial) and isotropisation. It should be noted that frequencies values have been chosen in order to provide a clearly distinction between the phase transitions.

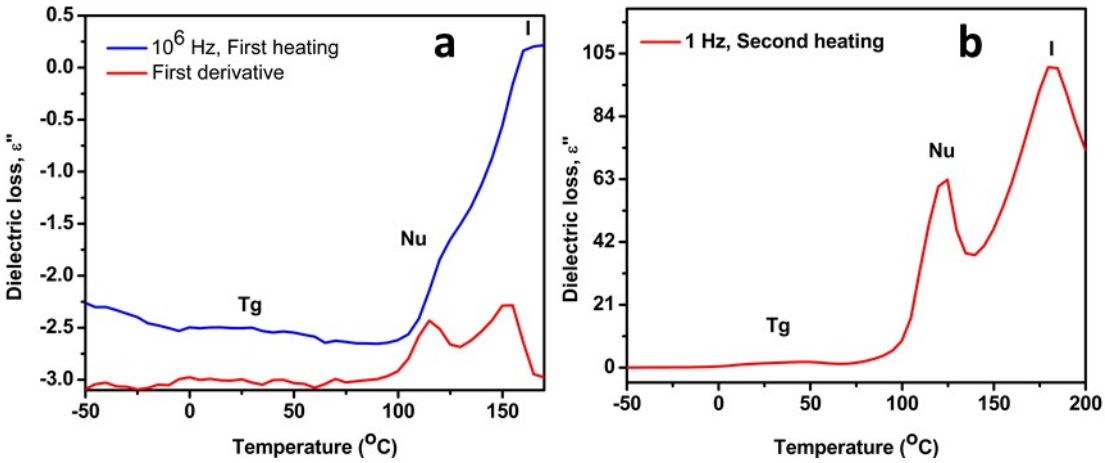

Figure S23. Phase transitions highlighted by dielectric spectroscopy for CuL^3 (a) and NiL^2 (b): Tg (glass transition), Nu (nematic uniaxial) and isotropisation. It should be noted that frequencies values have been chosen in order to provide a clearly distinction between the phase transitions.

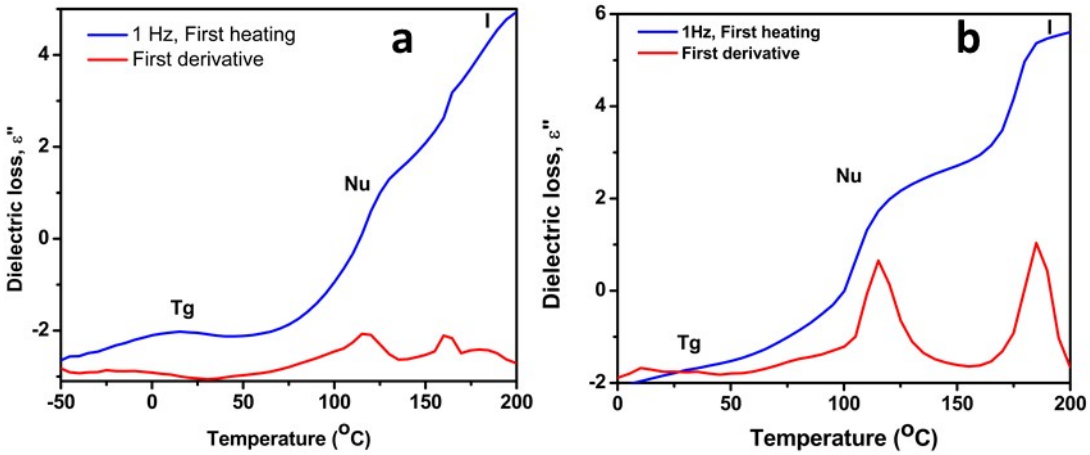

Figure S24. Phase transitions highlighted by dielectric spectroscopy for NiL^1 (a) and ZnL^1 (b): Tg (glass transition), Nu (nematic uniaxial) and isotropisation. It should be noted that frequencies values have been chosen in order to provide a clearly distinction between the phase transitions.

Tabel S4. Activation energies (eV) determinate by conductivity (S/cm) for crystal to nematic uniaxial phase transitions.

Frequency (Hz)	**CuL^1 First heating**	**CuL^1 Second heating**	**CuL^3 First heating**	**CuL^3 Second heating**
	Ea Cr-Nu (eV)	**Ea Cr-Nu (eV)**	**Ea Cr-Nu (eV)**	**Ea Cr-Nu (eV)**
1	1.32	1.41	0.42	0.48
10^1	1.25	1.37	0.41	0.44
10^2	1.09	1.12	0.32	0.41
10^3	0.88	2.02	0.20	0.39
10^4	0.61	2.10	1.55	0.60
10^5	0.42	1.45	1.54	0.58
10^6	0.37	1.01	1.42	0.46

Tabel S5. Activation energies, **Ea (eV)**, determined by conductivity **σ** (S/cm) for crystal to nematic uniaxial phase transitions.

Frequency (Hz)	CoL[1] First heating	CoL[1] Second heating	NiL[1] First heating	NiL[1] Second heating
	Ea Cr-Nu (eV)	Ea Cr-Nu (eV)	Ea Cr-Nu (eV)	Ea Cr-Nu (eV)
1	1.24	2.55	2.15	1.29
10^1	1.04	2.34	2.07	1.17
10^2	1.03	2.18	2.06	1.10
10^3	0.71	1.95	1.53	0.95
10^4	0.44	1.61	1.33	0.81
10^5	0.60	1.27	1.17	0.69
10^6	0.66	1.06	0.45	0.33

Tabel S6. Activation energies, **Ea (eV)**, determinate by conductivity **σ** (S/cm) for crystal to nematic uniaxial phase transitions.

Frequency (Hz)	NiL[2] First heating	NiL[2] Second heating	ZnL[1] First heating	ZnL[1] Second heating
	Ea Cr-Nu (eV)	Ea Cr-Nu (eV)	Ea Cr-Nu (eV)	Ea Cr-Nu (eV)
1	0.92	3.37	3.37	2.53
10^1	0.85	2.05	2.05	2.36
10^2	0.84	1.37	1.4	2.15
10^3	0.66	1.38	1.39	1.96
10^4	1.10	1.77	1.66	1.72
10^5	1.49	1.07	1.11	1.49
10^6	1.24	1.07	-	1.22

Amorphous vs crystalline statement

Tabel S7. Dielectric constant **ε'** and conductivity **σ** (S/cm) for complexes (25 °C, 1Hz) highlighting the higher values for second heating, respectively amorphous state.

Compound	First heating		Second heating	
	ε'	σ (S/cm)	ε'	σ (S/cm)
CuL[1]	2.67	1.15×10^{-15}	2.31	7.83×10^{-16}
CoL[1]	1.93	8.91×10^{-16}	4.63	3.11×10^{-15}
NiL[1]	2.23	4.97×10^{-15}	1.19×10^{2}	1.25×10^{-10}
ZnL[1]	2.76	9.12×10^{-15}	2.97	3.39×10^{-15}
NiL[2]	2.27	3.83×10^{-15}	2.99	4.12×10^{-15}
CuL[3]	2.04	2.81×10^{-15}	2.91	3.32×10^{-14}

Tabel S8. Dielectric constant **ε'** and conductivity **σ** (S/cm) for complexes (150 °C, 1Hz) highlighting the higher values for second heating, respectively amorphous state.

Compound	First heating		Second heating	
	ε'	**σ (S/cm)**	**ε'**	**σ (S/cm)**
CuL[1]	7.98	1.52×10^{-11}	7.46	4.67×10^{-11}
CoL[1]	3.25	2.81×10^{-12}	5.96×10^{1}	2.21×10^{-10}
NiL[1]	1.56×10^{1}	6.82×10^{-11}	3.66×10^{3}	2.96×10^{-8}
ZnL[1]	2.06×10^{1}	2.85×10^{-10}	5.31×10^{4}	3.3×10^{-4}
NiL[2]	5.44	1.08×10^{-11}	7.76	2.04×10^{-11}
CuL[3]	3.97×10^{2}	9.26×10^{-9}	4.18×10^{3}	3.64×10^{-8}

Tabel S9. Phase transition enthalpies, **ΔH (J/g),** on first heating and second heating (DSC). It can be observed the higher transition enthalpy for first heating, respectively crystalline state.

Compound	Heating			Cooling	
	First Heating		Second heating		
	ΔH (J/g)				
	Cr-Nu	**Nu-I**	**Cr-Nu**	**Nu-Cr**	**I-Nu**
CoL[1]	3.19	8.22	0.72	-0.25	-1.20
CuL[1]	74	4.37	1.39	-4.16	-4.42
ZnL[1]	38	6.3	0.65	-0.90	-0.50
NiL[1]	4.25	10.57	1.28	-0.47	-1.19
NiL[2]	1.11	4.88	0.54	-0.84	-1.11
CuL[3]	0.85	3.01	0.62	-	-

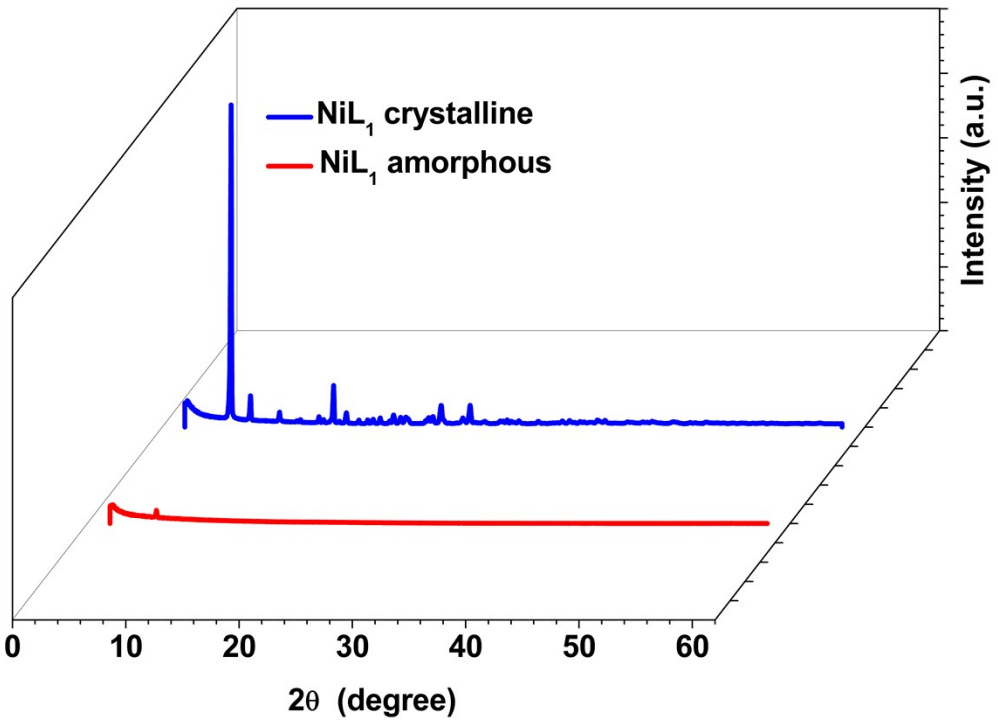

Figure S25. Comparison PXRD diffractograms of NiL^1 amorphous vs crystalline. The degree of crystallinity is 22.64% for crystalline powder and 2.35% for amorphous oil.

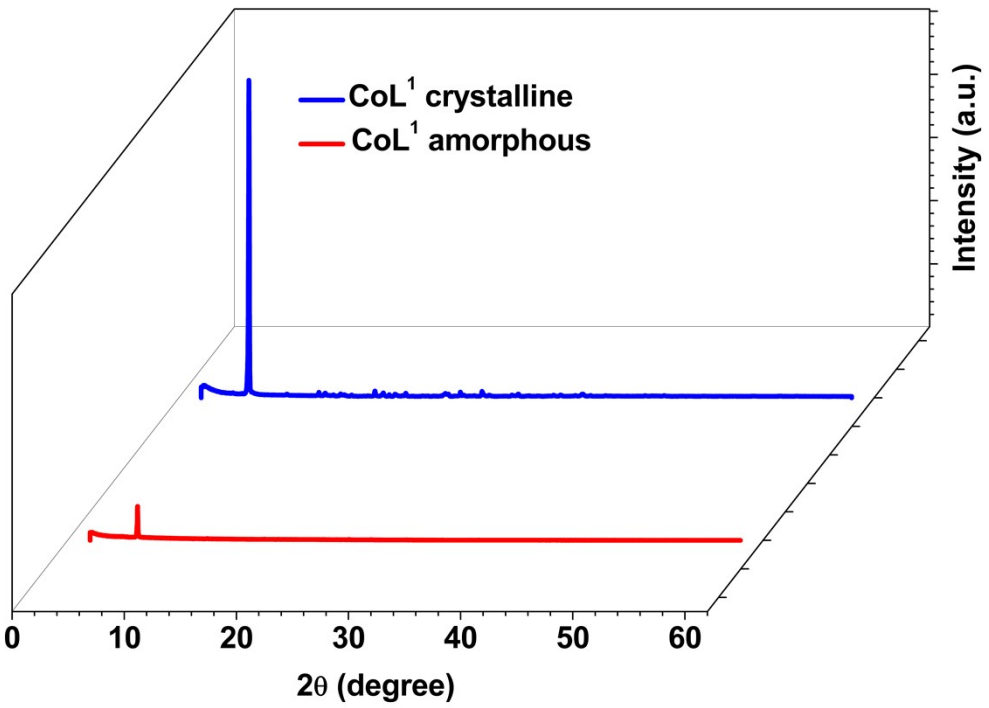

Figure S26. Comparison PXRD diffractograms of CoL^1 amorphous vs crystalline. The degree of crystallinity is 25.45% for crystalline powder and 5.64% for amorphous oil.

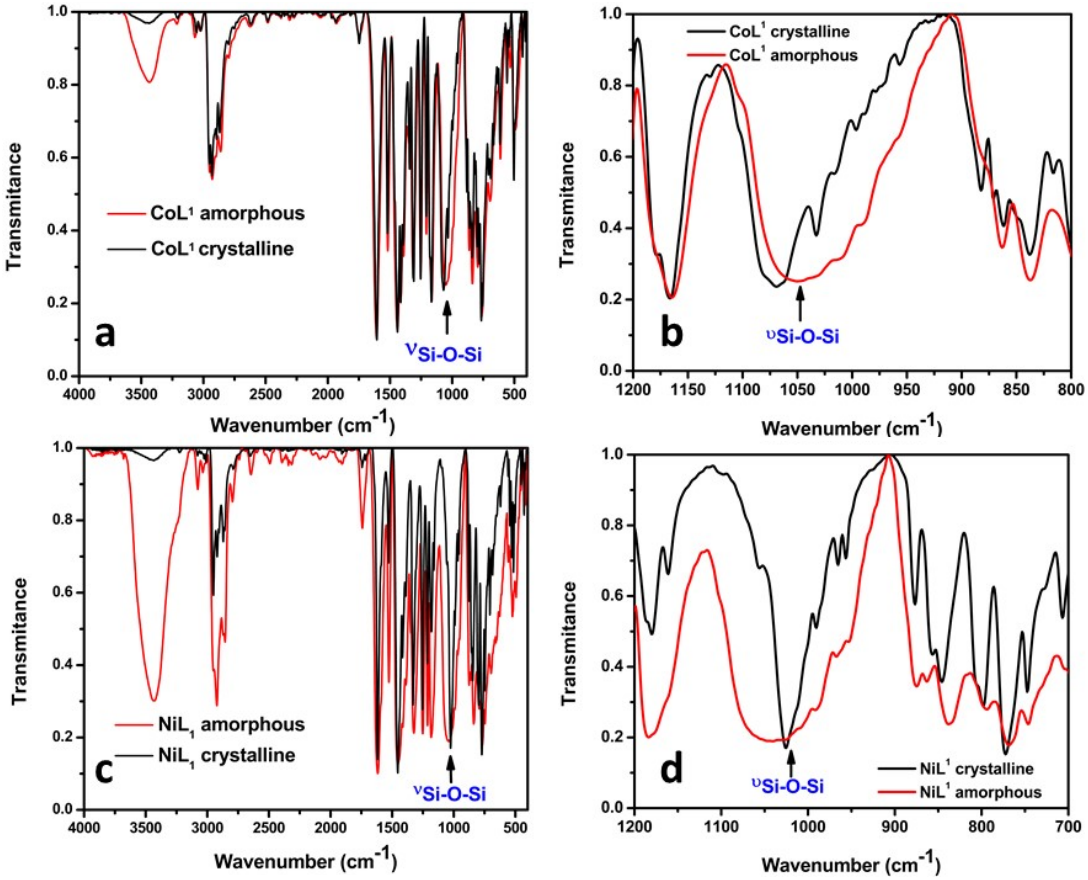

Figure S27. FTIR spectra of amorphous vs crystalline CoL^1 (a), (b) and NiL^1 (c), (d).

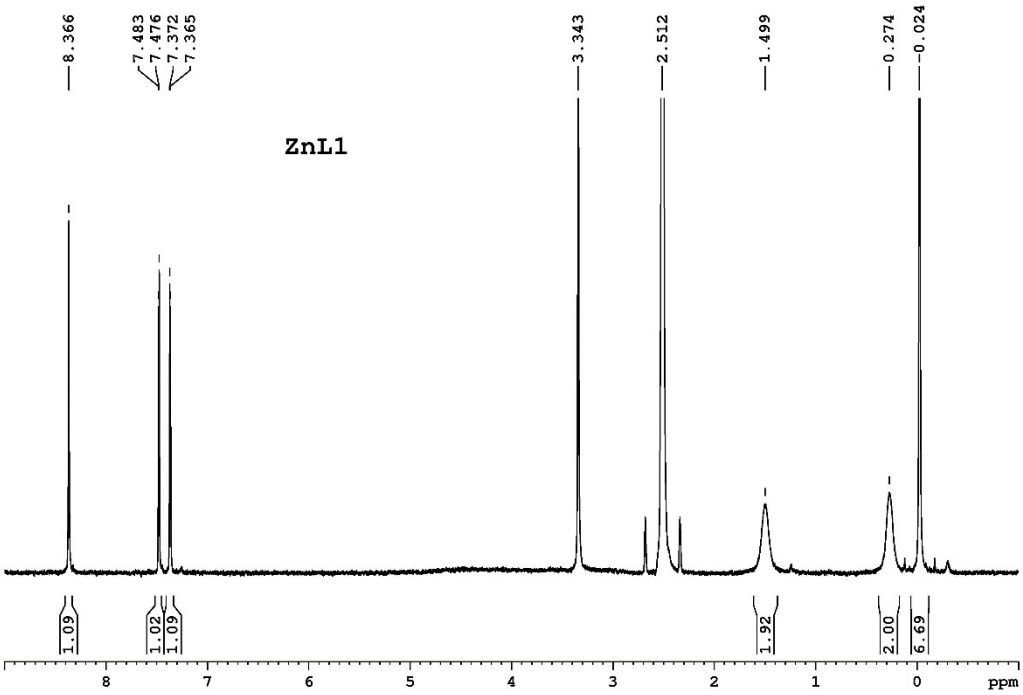

Figure S28. ^{1}HNMR spectrum for ZnL^1 after its izotropisation.

AIE features based on Thermotropic and Lyotropic LCs

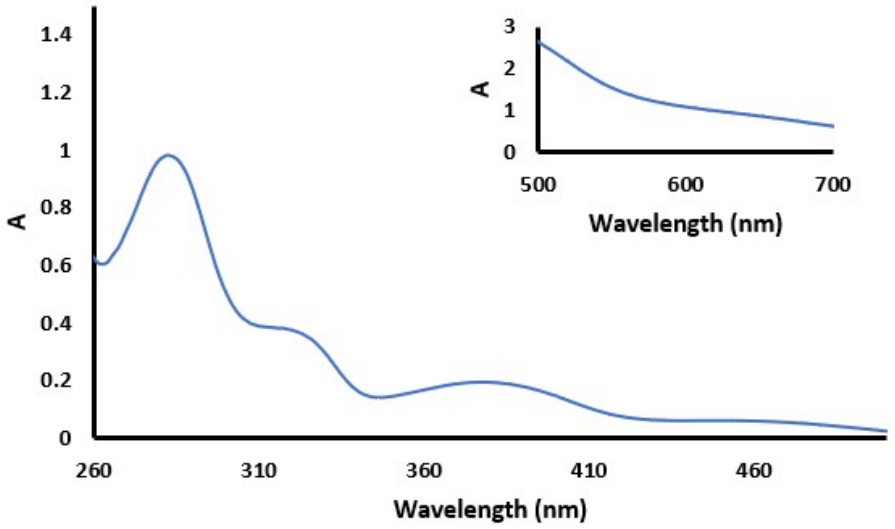

Figure S29. Absorption spectrum exemplified for CuL^3 in $5x10^{-5}$ M DMF solution. Upper right is observed d-d transition at higher concentration.

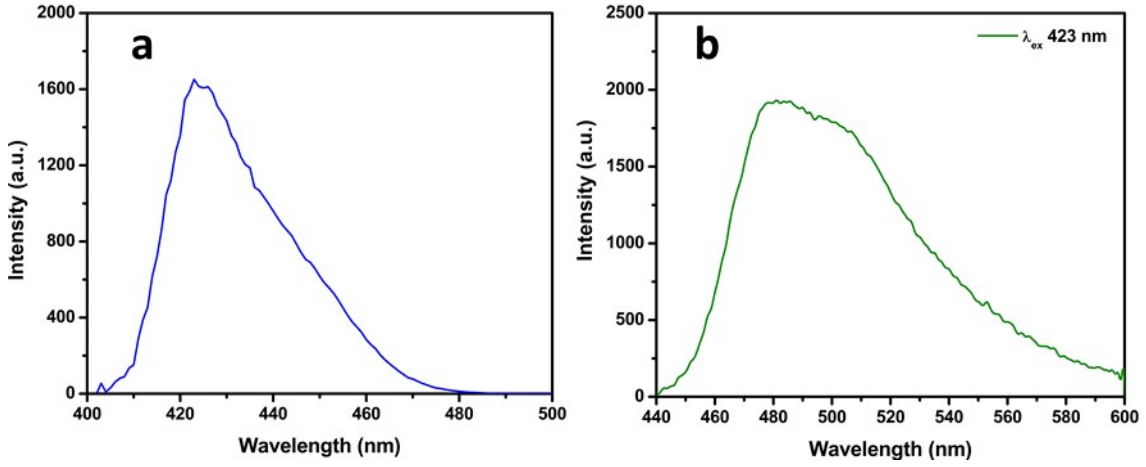

Figure S30. Excitation (a) and emission (b) spectra for NiL^1 DMF solution 10^{-3}M.

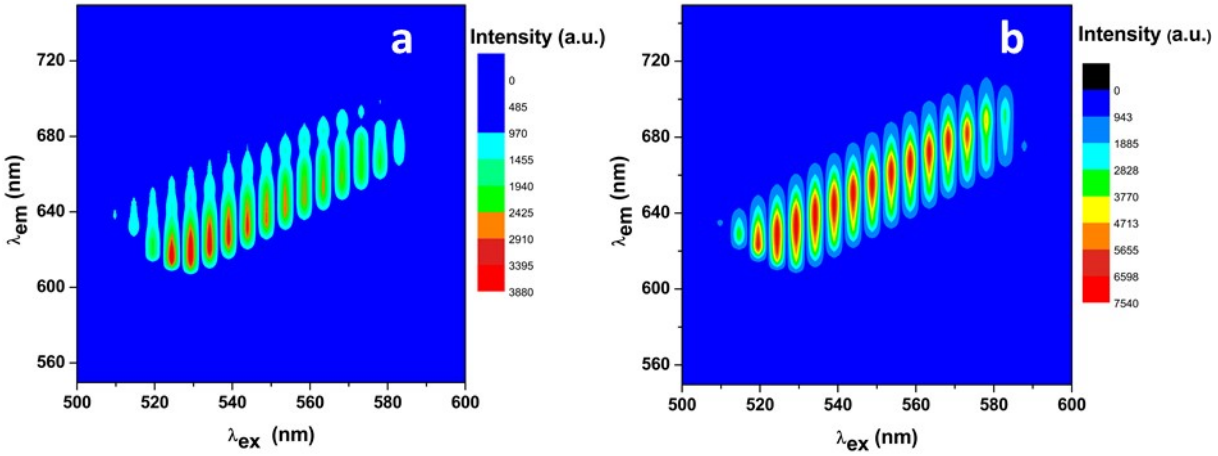

Figure S31. Excitation-emission matrix for thermotropic LC of CoL^1 (a) and CuL^1 (b). It should be noted that the minor signals in the range 600-700 nm have been removed for clarity.

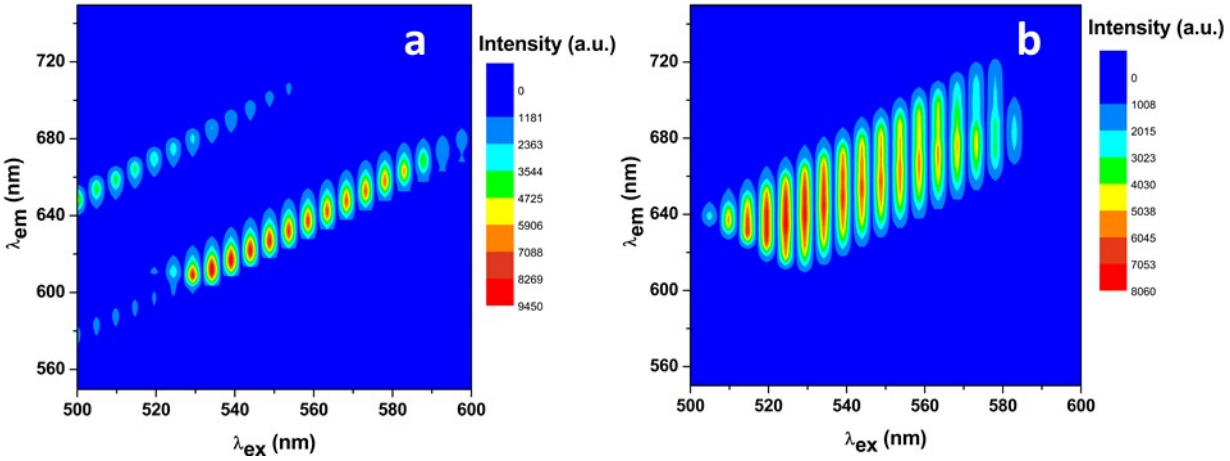

Figure S32. Excitation-emission matrix for thermotropic LC of NiL^1 (a) and NiL^2 (b). It should be noted that the minor signals in the range 600-700 nm have been removed for clarity.

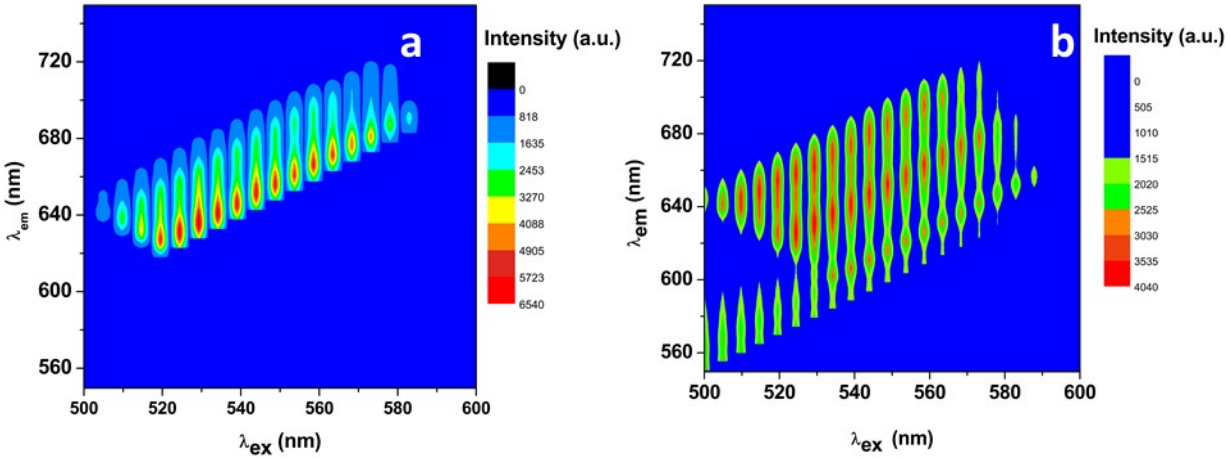

Figure S33. Excitation-emission matrix for thermotropic LC of CuL^3 (a) and ZnL^1 (b); It should be noted that the minor signals in the range 600-700 nm have been removed for clarity.

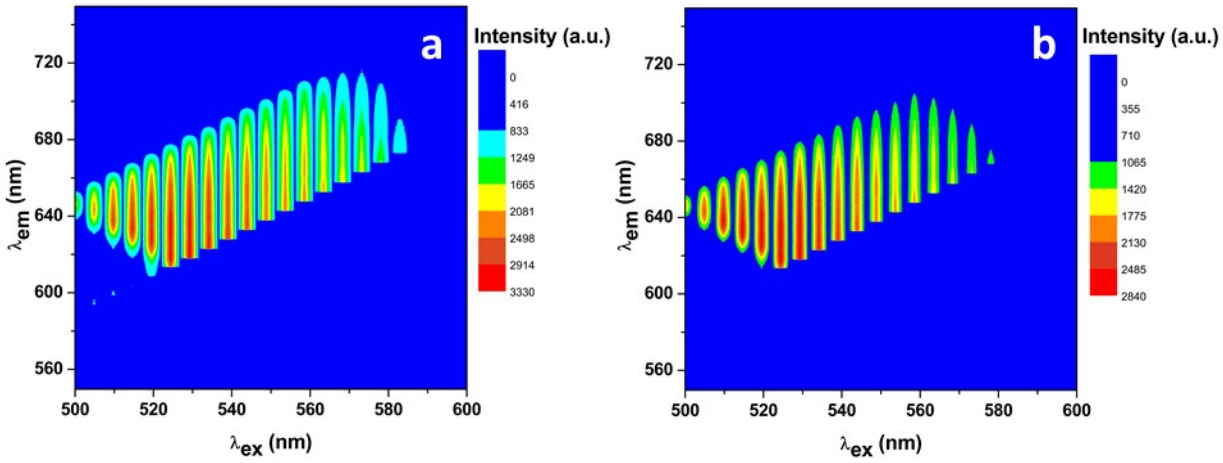

Figure S34. Excitation-emission matrix for lyotropic liquid crystals of CoL^1 (a) and of NiL^2 (b) 10^{-3} M. It should be noted that the minor signals in the range 600-700 nm have been removed for clarity and for correction of the inner effect absorbance was acquired.

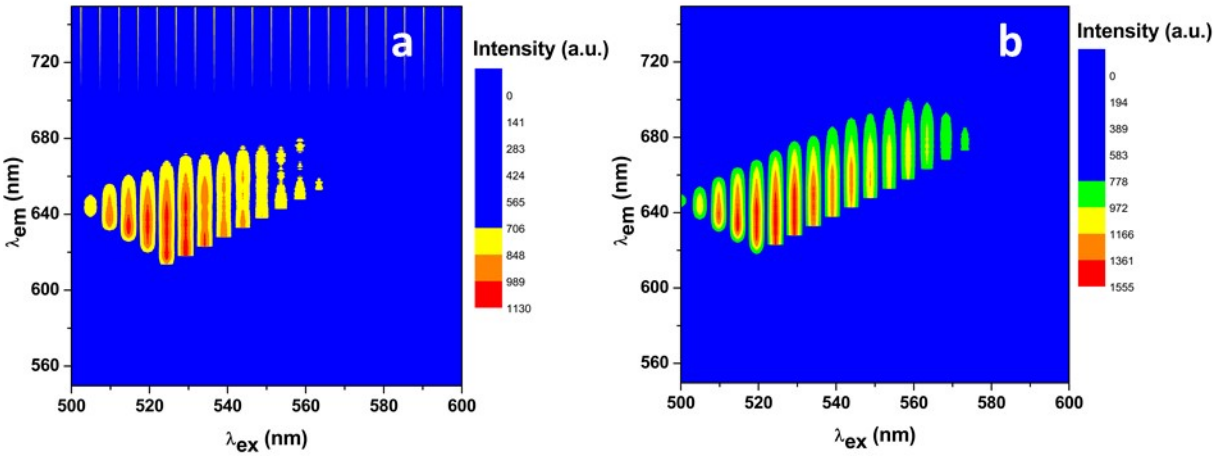

Figure S35. Excitation-emission matrix for lyotropic liquid crystals of NiL^1 (a) and of ZnL^1 (b) 10^{-3} M. It should be noted that the minor signals in the range 600-700 nm have been removed for clarity and for correction of the inner effect absorbance was acquired.

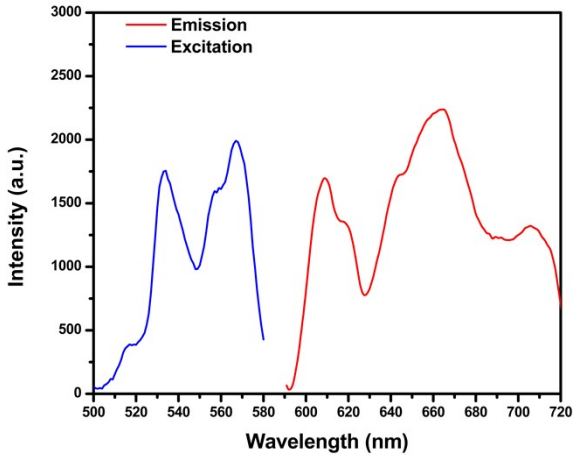

Figure S36. Mirror image of the ZnL^1 solid crystalline powder indicating a vibronic structure.

Tabel S10. Excitation and emission wavelengths in the case of thermotropic and lyotropic LCs.

Compound	Lyotropic LCs		Thermotropic LCs	
	Λex (nm)	Λem (nm)	Λex (nm)	Λem (nm)
CoL^1	533	573; 609; 626; 697	534	585; 604; 622; 660; 724
CuL^1	535	573; 610; 681	538	583; 597; 644; 696
NiL^1	532	569; 623; 656	533	594; 608; 681; 733
ZnL^1	533	574; 609; 628; 679	533	577; 607; 625; 672; 734
NiL^1	533	572; 609; 626; 679	531	572; 605; 643; 687; 719
CuL^3	533	572; 608; 626; 682	532	568; 607; 644; 720

Supramolecular alignment

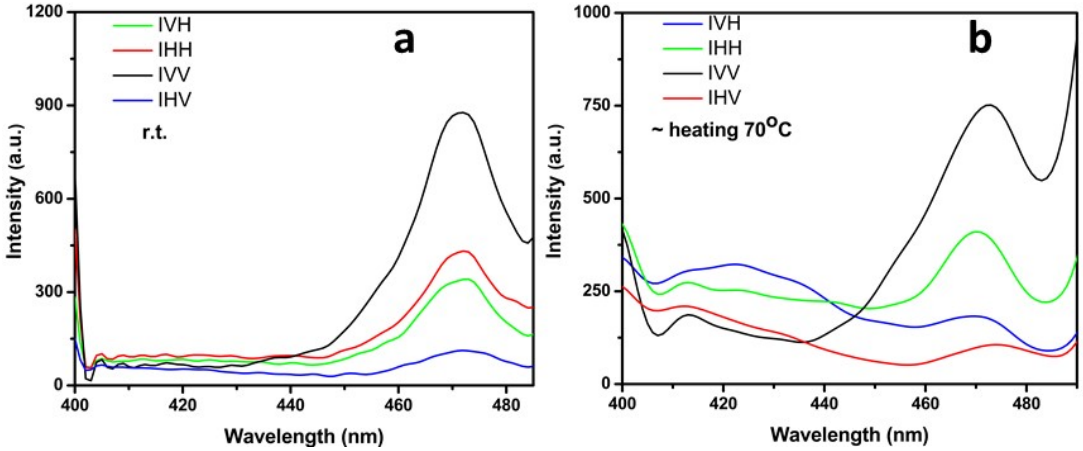

Figure S37. NiL^1 lyotropic liquid crystals excitation spectra with vertically and horizontally polarized light at room temperature (a) and by heating (b).

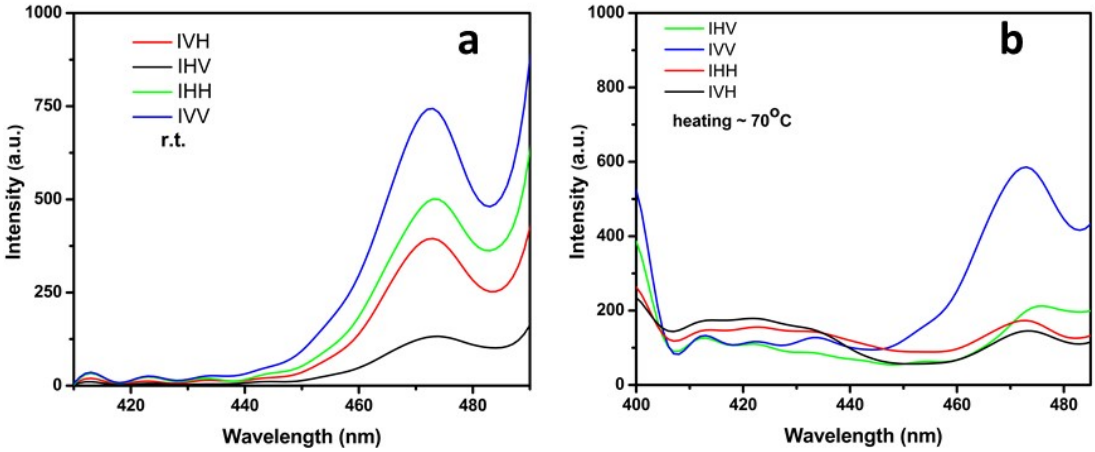

Figure S38. NiL^2 lyotropic liquid crystals excitation spectra with vertically and horizontally polarized light at room temperature (a) and by heating (b).

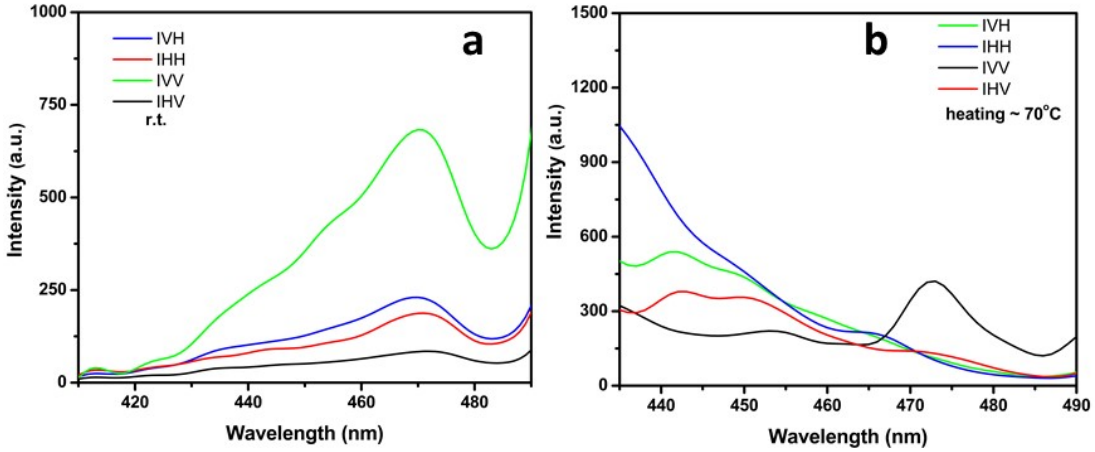

Figure S39. CoL^1 lyotropic liquid crystals excitation spectra with vertically and horizontally polarized light at room temperature (a) and by heating (b).

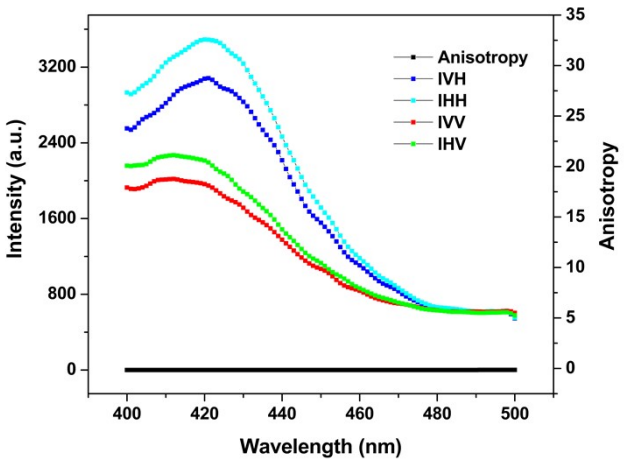

Figure S40. Anisotropy and excitation spectra exemplified for NiL^1 at high temperatures around 90 ^oC showing randomly distribution of molecules without any orientational order.